DR NADICA D. ABAZOVIĆ (Orcid ID : 0000-0003-0718-5186)

Article type : Article

Binary oxide ceramics for enhanced phenols degradation under simulated Solar light

Milica V. Carević[1], Nadica D. Abazović[1*], Tatjana D. Savić[1], Tatjana B. Novaković[2], Dejan J. Pjević[1], Mirjana I. Čomor[1*]

[1]Vinča Institute of Nuclear Sciences, University of Belgrade, P. O. Box 522, 11001 Belgrade, Serbia

[2]IChTM- Department of Catalysis and Chemical Engineering, University of Belgrade, Njegoševa 12, 11000 Belgrade, Serbia

[*]***Corresponding authors***: Dr. Mirjana I. Čomor and Dr. Nadica D. Abazović, Phone: +381113804192; Fax: +381113408607; Vinča Institute of Nuclear Sciences, University of Belgrade, P.O. Box 522, 11001 Belgrade, Serbia: e-mail address: mirjanac@vin.bg.ac.rs; kiki@vin.bg.ac.rs

Abstract

Solvothermal synthesis of ZrO_2-TiO_2 binary oxides and pure counterparts at 150 ^{o}C in water/isopropanol media is presented. Titanium (IV) isopropoxide and zirconium (IV) propoxide were used as precursors. XRD and TEM techniques were used for structural and morphological characterization of obtained samples. XPS spectra of mixed oxide samples were compared in order to correlate composition of samples with surface properties and presence of defects. Relative positions of defect states within band-gaps of semiconductors were estimated from UCPL spectra. UV-Vis DRS spectra revealed that both pure oxides experienced red shift of absorption thresholds compared to reference data. Photocatalytic activities of all samples were probed under simulated solar light on three model compounds: phenol, 4-chlorophenol (4-CP) and 2, 4, 6-trichlorphenol (TCP). Pure TiO_2 showed the highest photocatalytic activity in the case of phenol. However, pure ZrO_2 and binary oxides showed higher photoactivity in degradation of 4-CP and TCP. The activity of wide band-gap semiconductors under simulated Solar light in photodegradation of phenol and its derivatives is most probably the consequence of formation of charge transfer complexes between pollutant molecules and semiconductors surface.

Keywords: ceramics; oxide materials; optical properties; photoelectron spectroscopies; transmission electron microscopy, TEM

1. Introduction

Humanity is facing a huge environmental risk due to increasing contamination of the surface and ground waters. Textile dyes, various pesticides and newly emerging contaminants like pharmaceuticals and personal-care products, are a major threat for the freshwater systems.[1] Finding an inimitable method to diminish or eliminate the effects of these organic pollutants is a must. One of the methods that offer a solution for degradation of all these pollutants is certainly semiconductor heterogeneous photocatalysis.[2,3] The semiconductor by itself must meet certain requirements in order for its usage for environmental protection to be justified: it must be cheap, widely abundant and above all, not toxic for the environment.[2,3]

TiO_2 is a well-known semiconductor with a potential for wide applications in all fields where light-semiconductor interaction is needed (photocatalysis, photovoltaics, etc.). It has many advantages like high efficiency, biological and chemical stability, non-toxicity and low cost, but there are also a few major disadvantages of this material. One of them is certainly the fact that due to its wide band gap (about 3.2 eV), it absorbs in the UV region of Solar spectrum, and that is just about 5% of light that reaches the Earth's surface. Many efforts have been made to manipulate the band-gap of TiO_2 in order to move its spectral response deeper in the visible part of the spectrum. Doping with transition metal ions is a common method to achieve this improvement [4,6]. It leads to the formation of new levels in the band-gap of TiO_2, and consequently enables photons with energies lower than that of the semiconductor's band-gap to produce electron-hole couples. A similar effect can be achieved by modifying the surface of TiO_2 through its interaction with certain organic molecules [7-9] when charge-transfer complex formation takes place, but then its surface becomes occupied and unavailable for heterogeneous degradation of pollutant molecules.

Even when charge carriers are formed, they need to stay separated in order to later participate in the reduction/oxidation reactions on the semiconductor surface. Coupling TiO_2 with other metal oxides can postpone recombination and prolong the life of photogenerated charge carriers. Until now, TiO_2 was coupled with various metal oxides, like SiO_2, [10,11] Al_2O_3, [12,13] ZnO, [14] Bi_2O_3 and V_2O_5 [15]. Lately, even if it is characterized with a wide band-gap, ZrO_2 became very interesting for this purpose. Bulk zirconia has a band-gap energy of about 5.0 eV [16] which means that it absorbs the UVC spectral region. It is an *n*-type semiconductor with 4*d* states placed at potential more negative (-1 V, NHE) than that of the conduction band minimum and valence band at potential more positive (4 V, NHE) than the valence band maximum of TiO_2 (about -0.1 V, and 3.1 V, NHE, respectively) [16]. In a scenario where ZrO_2 and TiO_2 particles are in close contact, such relation of potentials of conduction and valence bands can provide transfer of photogenerated charges from one semiconductor to another, and subsequently prevent their recombination. It is also reported [17] that the specific surface area of mixed oxide is higher than that of the initial, pure constituent oxides. A larger surface area means a higher possibility for adsorption of pollutants, but also of oxygen from the surroundings which through reaction with photogenerated electrons can be transformed into highly reactive superoxide radical anion ($O_2^{-\bullet}$). Moreover, addition of ZrO_2 leads to the increase of surface acidity in the form of OH^- groups. Through reaction with photogenerated holes, OH^- groups are transformed to $OH^\bullet$ radicals. Presence of both radical species is highly desirable in photocatalytic processes since both are strong agents that can degrade a wide palette of organic pollutants.

TiO_2-ZrO_2 mixed oxides have been synthesized by various techniques: controlled hydrolysis[18], ionic-liquid route[19] and co-precipitation method [20], but mainly by sol-gel methods [21-25]. Common points for all indicated methods are that the obtained samples were annealed after synthesis, and that UV light was used to photoactivate the semiconducting materials.

As far as we know, only Kiwi with his group [26,27] have used Solar light to photoactivate TiO_2-ZrO_2 mixed oxides in reactions of methylene-blue (MB) decolorisation and bacterial (*Escherichia coli)* inactivation.

In the scope of this study, we synthesized a series of TiO_2-ZrO_2 (TZ) mixed oxides using solvothermal method. By using this method, we were able to produce highly crystalline samples, and avoid the need for their subsequent calcination which can decrease the number of OH^- groups at samples' surface. Photocatalytic activity of TZ samples was probed on photodegradation of model compounds: phenol, 4-chlorophenol (4-CP) and 2, 4, 6-trichlorphenol (TCP), common environmental contaminates[28]. Samples were photoactivated using simulated Solar light.

2. Experimental

2.1. Materials

All chemicals were of analytical grade (highest available) and were used without further purification. The following commercial chemicals were used: Titanium (IV) isopropoxide (TTIP, Aldrich, ≥97%), Zirconium (IV) propoxide (ZIP, Sigma-Aldrich, 70 wt% solution in 1-propanol), phenol (Sigma – Aldrich, ≥99%); 4-chlorophenol (4-CP, Alpha Aesar, 99%) and 2, 4, 6-trichlorophenol (TCP, Alpha Aesar, 98%), nitric acid (J.T. Baker, 65%), isopropanol (J.T. Baker, >99.8%) and methanol (J.T. Baker, HPLC grade). Deionized water from the Mili Q system was used in all the experiments.

2.2. Sample preparation

Pure and mixed binary oxide nanopowders were synthesized by solvothermal treatment. In a Teflon vessel (125 ml volume) 25 ml of water and 20 ml of isopropanol were mixed at ~ 0 °C. pH was adjusted to ~2, by using nitric acid. Then, in order to get the denoted TiO_2/ZrO_2 % ratio, appropriate amounts of TTIP and ZIP (Table 1) were added dropwise, simultaneously, while the solvent mixture was vigorously stirred. After 15 min of stirring in an ice bath, the dispersion was autoclaved 24 h at 150 °C. The obtained powders were washed using water until the water reached pH = 6. Finally, the powder was separated from the washing solution by centrifugation and dried at 100 °C until a constant weight was reached. Obtained samples were denoted as TiO_2, ZrO_2, TZ25 (TiO_2/ ZrO_2=75/25), TZ50 (TiO_2/ ZrO_2=50/50) and TZ75 (TiO_2/ ZrO_2=25/75).

Table 1. Amounts of TTIP and ZIP used for oxides synthesis

2.3. Sample characterization

The XRD powder patterns were obtained using a Philips PW 1050 powder diffractometer with Ni filtered Cu K_α radiation (λ = 1.5418 Å). The diffraction intensity was measured by the scanning technique (a step size of 0.05° and a counting time of 50 s per step). The average crystallite size (D in nm) was determined from XRD patterns according to the Scherrer equation (1):

$$D=k\lambda/\beta\cos\theta \qquad (1)$$

where k is a constant equal to 0.89, λ is the X-ray wavelength equal to 1.5418 Å, β is the full width at half the maximum intensity (FWHM) of the most intensive peak of the obtained crystalline phase, and θ is the diffraction angle (rad) of the same peak.

The morphology and sizes of photocatalysts nanoparticles were obtained using transmission electron microscopy, TEM, JEOL JEM 1400, accelerating voltage 120 kV. Samples for TEM analysis were prepared as follows: a small quantity of powder was dispersed in methanol, ultrasonicated for 1 h, deposited on C-coated Cu grids.

Textural properties of synthesized samples were determined using automatic adsorption apparatus Sorptomatic 1990 Thermo Finningen. As obtained nitrogen adsorption/desoption isotherms were used to calculate standard textural parameters of synthesized materials by applying BET method [29-31]. Detailed experimental conditions are given in Supplementary Materials available online.

XPS analyses were carried out on the PHI-TFA XPS spectrometer manufactured by Physical Electronics Inc. XPS spectra were excited by X-ray radiation from an Al-monochromatic source. The binding energy of XPS spectra was calibrated in the way that within the spectrum of carbon C 1s, the peak typical of the chemical bonds C-C/C–H was set at the binding energy 284.8 eV.

UV/Vis reflectance spectra (DRS) of obtained powders were obtained using an Shimadzu UV-2600 spectrophotometer (Shimadzu Corporation, Tokyo, Japan) equipped with an integrated sphere (ISR-2600 Plus (for UV-2600)). Photoluminescence measurements were performed using Perkin-Elmer LS 45 fluorescence spectrometer.

2.4. Photodegradation and analytical procedure

Photocatalytic degradation of phenol, 4-CP and TCP aqueous solutions on synthesized samples was carried out using simulated Solar light. Experimental set-up was previously described by Radoičić et al.[32]; details are given in Supplementary Material.

For kinetic studies of phenol, 4-CP and TCP photodegradation, high performance liquid chromatography (HPLC) with diode array detection was used, as previously described by Carević et al.[33]. Detailed adsorption (Figure S1), photodegradation and analytical procedures are presented in Supplementary Materials available online.

3. Results and discussion

3.1. Structure and morphology

XRD patterns of the synthesized samples are presented in Figure 1. Pure TiO_2 (Figure 1a) crystalizes in anatase (A) crystal form (JCPDS 21-1272) [18], with a small additional content of brookite phase (peak at about 30.7º, indicated as B in Figure 1a). Photocatalytic activity of TiO_2 strongly depends on its structural properties, such as its crystalline structure and phase content. Titanium dioxide exists in three main crystallographic forms: anatase, rutile, and brookite, with band gap energies of 3.2, 3.02 and 2.96 eV, respectively. Anatase and rutile have a tetragonal structure and they are widely used for photocatalytic applications. Brookite has orthorhombic structure and it is the least studied titanium dioxide phase [34]. The rutile form is the most stable polymorph of TiO_2, while the anatase form is metastable and transforms irreversibly to rutile at elevated temperatures. [35] However, it is well known that anatase TiO_2 usually shows higher photoactivity then the rutile TiO_2 while mixtures of these two phases show better photocatalytic activity than the pure ones. [36] By applying Scherrer equation on (101), the most intensive peak of anatase crystalline phase (at ~25.4°), it was calculated that average crystal domain size is about 6 nm.

Pure ZrO_2 (Figure 1e) mainly crystalizes in a metastable tetragonal (T, ~ 80 %) crystal form (JCPDS 81-1544), but low-intensity peaks that originate from monoclinic (M, ~ 20%) (JCPDS 65-1025) crystalline structure can also be seen. The metastable tetragonal crystalline structure is stable up to 650 °C [37], and the monoclinic phase is stable from room temperature to 1200 °C [38]. Besides temperature demands, transition from *m*T to M phase is possible at lower temperatures if particle size reaches app. 30 nm. [39] Since both phases are existing, that can be indication that under given experimental conditions wide particle size distribution is present. As the most intensive peaks of *m*T and M phases are very close, the obtained peaks need to be fitted in order to apply the Scherrer equation to calculate the average crystal domain size of these two phases.[38] We obtained diameters of about 10 nm for monoclinic and 8 nm for *m*T crystalline phases; these sizes should be considered only as approximation.

Characteristic diffraction peaks of both oxides are clearly visible in XRD patterns of binary oxides (Figure 1 b-d). Intensity ratio between (101) peak of anatase phase of TiO_2 and (101) peak of *m*T phase of ZrO_2 follows the stoichiometric ratio of these two binary oxides. It is also interesting to notice that, regarding intensities of (101) peak of *m*T and (-111) peak of M phase, their mutual ratio does not change with increasing the amount of TiO_2 in the binary oxide sample.

Figure 1. XRD patterns of pure and binary oxides

TEM images (Figure 2) gave us better insight in the particle size distribution and morphology of the samples. Anatase TiO_2 (Figure 2a) has a mixed morphology, since both spherical and faceted cube-like particles are observed. It was previously reported [40] that in solvothermal synthesis, alcohols can act as capping agents, and, depending on the nature of the alcohol used, stabilize the (101) or (011) facet of TiO_2. We believe that here isopropanol acted as a stabilizing agent, causing partial cubical morphology of TiO_2 nanoparticles. Depending on which facet is exposed, photocatalytic activity of TiO_2 will change, due to different electrophilic character and coordination number of Ti cations on different facets.[41] Even though the nanoparticles are agglomerated, it was possible to determine that the average particle size is about 7 nm, which is in fair accordance to the XRD findings.

Figure 2. TEM images of synthesized oxides: a) TiO_2, b) ZrO_2, c) TZ25, d) TZ50 and e) TZ75

Like TiO_2, pure zirconia sample (Figure 2b) is characterized with various morphologies: from spherical particles of about 2 nm to large irregularly shaped particles of about 30 nm. As we have mentioned earlier in the text, *m*T to M phase transformation of zirconia demands sizes of at least ~30 nm [39]. According to the TEM images, this fraction of the particles is present to a very small content in the sample, which is in good accordance with the XRD findings.

As TEM images of binary oxides (Figure 2c and d) revealed, the two oxides didn’t affect each other’s morphologies and sizes. It might be concluded that isopropanol doesn’t have the same capping and stabilizing effect on zirconia particles like it has on titania particles. There is no competition between the two: upon mixing, titania particles stay faceted, while zirconia is still characterized with spherical particles and wide particle size distribution. Even though Ti and Zr cations have similar ionic radii (0.68 and 0.84 Å, respectively), and the same charge, the main difference between the two is in the way they are packed in a crystal lattice of the corresponding oxide. Namely, Zr^{4+} is octacoordinated in t-ZrO_2 and seven-fold coordinated in m-ZrO_2.[42] TiO_2 is made from TiO_6 units, where it is hexacoordinated, but for particles smaller than 20 nm, surface Ti atoms are pentacoordinated, feature that is actually convenient in surface modification of TiO_2, since it provides easier ligand binding.[7] This difference may be a reason for the different growth path in the same synthesis conditions.

3.2. Textural properties

Nitrogen adsorption-desorption isotherms (Figure 3a) were used to determine textural properties of the obtained samples. Specific surface areas (S_{BET}), pore volumes ($V_{p\ 0.98}$) and pore sizes are summarized in Table 2.

Table 2. Textural properties of synthesized oxides

Figure 3. a) N_2 adsorption/desorption isotherms and (b) pore size distributions patterns of synthesized oxides.

The isotherms of all samples can be classified as IUPAC type IVa with H2-hysteresis loop, characteristic for mesoporous materials. The p/p_0 at the starting point of the adsorption curve increment is directly related to the porous dimensional structure[31]. For all isotherms, this inflection point is suited at $p/p_0 \sim 0.5$, indicating a capillary condensation of gaseous N_2, which further implies a narrow porous size distribution [31], as is also confirmed by our measurements (Figure 3b). $V_{p\ 0.98}$ value is lowest for pure zirconia, and highest for pure titania. S_{BET} follows a similar trend, with the exception of the sample TZ50, which has a specific surface lower than pure zirconia. Our results are in opposition with literature data, since one of the reasons for titania-zirconia coupling was to increase the specific surface area of obtained coupled oxide.

3.3. Surface structure

In order to compare surface composition of nanocomposites with lowest (TZ25) and highest (TZ75) zirconia content, XPS spectra were obtained (Figure 4 and survey spectra in Figure S2, peak assignment in detail is presented in Table S1).

The quantity of added ZrO_2 has significant influence on the state of the binary oxides surface. The binding energies of Ti 2p3/2 and Ti 2p1/2 are at 458.8 and 464.4 eV respectively, in both samples (Figure 4a and b), and they are characteristic for pure TiO_2. However, there are additional peaks in both samples, suited between 455 and 458 eV that indicated the presence of defect states (Ti^{2+} and Ti^{3+})[43] as well as at about 462 eV that originate from Ti_2O_3. Contribution of these species in Ti 2p area varies from ~30% for TZ75 to almost 50% for TZ25. Finally, formation of mixed Zr-Ti species is confirmed with presence of peak at 460.7 /459.8 eV that originate from TiO_2 – Zr bond [26,27] and peak between 466.5 and 468 eV which originate from $ZrTiO_4$[43].

In Zr 3d (Figures 4c and d) binding energy range, there are two main peaks for both samples at 182.5 and 185.2 eV, that originate from Zr $3d_{5/2}$ and Zr $3d_{3/2}$ spin orbit splitting, but also there is a peak at 180.7 eV which can be assigned to suboxidation states of zirconium ions (Zr^{+}, Zr^{2+} and Zr^{3+})[44].

Figure 4. XPS spectra and their deconvolutions of the characteristic energy ranges: Ti 2p binding energies for TZ25 (a) and TZ75 (b), Zr 3d energy ranges for TZ25 (c) and TZ75 (d) and O 1s binding energy ranges for TZ25 (e) and TZ75 (f).

The O 1s binding energy is presented in image Figures 4e and f. As expected, peaks of both samples are wide and asymmetric indicating the presence of different oxygen species, which is in accordance with previously stated presence of cation suboxidation species. The main peak is suited at 530.3 eV and it is assigned to lattice oxygen; peaks at lower binding energies suited between 526.5 and 529.5 eV can be assigned to oxygen bound to cations suboxidation species, while the peak suited at higher energy can be attributed to oxygen from surface hydroxyl groups [19]. Ratio between the area under this peak and the total area of O 1s can be used as a measure of the amount of surface hydroxyl groups. According to our findings, the sample with larger titania content TZ25 has a larger amount of surface hydroxyl groups (30%) than the sample with a larger zirconia content TZ75 (14%).

3.4. Optical properties

UV-vis diffuse reflectance spectra of all the synthesized samples were recorded in order to gain a deeper insight into the influence of oxides coupling on their electronic structure (Figure 5a).

As expected, the absorption edge of pure ZrO_2 was situated deep in the UV region. However, the absorption edge of pure TiO_2 was slightly shifted to longer wavelengths, while the absorption edges of coupled oxides were almost overlapped, and regardless of the share of ZrO_2 in the nanocomposite, close to that of pure TiO_2. For easier comparison, the obtained spectra were transformed to absorption spectra by using Kubelka-Munk functionality and to

Tauc's plots (inset in Figure 5a). Extrapolation of the linear part of plots gave information about band-gap energies of all samples. The estimated band-gap energy of pure ZrO_2 is 4.1 eV and well below the value of bulk band-gap (5.0 eV)[16]. This shift towards lower energies is also present for the band-gap of pure TiO_2 and coupled oxides, moving them closer to the visible spectral region. For pure TiO_2 this value is 3.0 eV, while it is estimated to be 3.1 eV for coupled oxides.

Figure 5. a) DRS spectra (inset: Tauc plots); b) PL spectra and c) UCPL spectra of synthesized oxides.

PL spectra of all synthesized oxides (Figure 5b) are characterized with a strong peak at about 420 nm (2.95 eV), with additional broad bands from 300 to 350 nm and from 430 to 470 nm. According to literature data, the energy of the most intensive transition corresponds to the lowest indirect transition $X_{1a}\rightarrow\Gamma_{1b}$ of TiO_2.[45] However, the same peak exists in the PL spectra of pure ZrO_2. As Wang et al. stated [46], there are two possible mechanisms that can explain the origin of emission in ZrO_2: a) existence of an impurity luminescence centre (ILC) and b) structure defect (SD) model. ILC model ascribes luminescence to the presence of Ti^{4+} impurity in ZrO_2 structure, while SD model claims that luminescence originates from singly ionized oxygen vacancies.[46] In order to clarify the origin of luminescence in synthesized samples, up-conversion photoluminescence (UCPL) spectra were recorded. Namely, if a semiconductor is irradiated with the energy lower than the band-gap energy, electrons from the valence band will be excited to levels situated below the conduction band. Upon their de-excitation to ground state, photons will be emitted, and UCPL spectra will be characterized with peaks at energies that correspond to energies of additional/defect levels.[45]

UCPL spectra of all the samples are presented in Figure 5c. Visible light with the wavelength of 560 nm (2.21 eV) was used for sample excitation which is well below the band-gap energy of both oxides, while spectra were recorded in the range from 320 to 510 nm (3.87 to 2.43 eV). All UCPL spectra are characterized with the presence of four peaks/shoulders suited at 402 nm (3.08 eV), 422 nm (2.94 eV), 447 nm (2.77 eV) and 484 nm (2.56 eV). Transitions at 402 nm and 422 nm are previously reported for polyvinyl stabilized *t*-ZrO_2 nanoparticles of 2 nm,[47] but also for oleic acid and oleylamine stabilized *m*-ZrO_2 nanoparticles of 4 and 5 nm.[48] Obviously, these transitions cannot be associated to crystal phase or size of nanoparticles. However, both transitions are also noticed in TiO_2 nanoparticles,[45] and they are assigned to indirect transitions; the peak at 402 nm corresponds to $\Gamma_{1b} \rightarrow X_{2b}$ transition, while the peak at 422 nm, as we have mentioned earlier, and corresponds to $X_{1a} \rightarrow \Gamma_{1b}$ transition. Transitions at 447 nm and 484 nm are associated to shallow trap levels that originate from oxygen vacancies. Additionally, in UCPL spectrum of pure zirconia there is a peak suited at 350 nm (3.54 eV), which, according to Carvalho et al.[49] originates from d-d transition of Ti^{3+} impurity in tetragonal ZrO_2.. What we can conclude here, is that the luminescence of ZrO_2 cannot be exclusively ascribed neither to the ILC nor the SD model, considering that both, naturally present Ti impurity and oxygen defect states, contribute to this luminescence simultaneously. As can be concluded, UCPL spectra confirmed XPS findings of lattice structure imperfection and presence of cation suboxidation species and oxygen vacancies.

3.5. Photocatalysis

In the majority of studies regarding binary oxides used as photocatalysts, they are combined in order to improve the separation of photogenerated charge carriers, and consequently, the ability of the material to produce OH radicals used in photodegradation processes. TiO_2/ZrO_2 nanocomposites are synthesized bearing in mind relative positions of the conduction and valence bands of pure components. Kambur et al.[22] have shown that the

CB edge of ZrO_2 is on more negative potential than that of TiO_2, and in the case of close contact of the two oxides, photogenerated electrons from ZrO_2 will be transferred to the CB of TiO_2. However, as ZrO_2 is a wide band-gap semiconductor UVC light is needed for its direct photoexcitation. As UV light makes less than 5% of Solar light, it is reasonable to presume that the process of charge separation will not be significant in a system where natural or simulated Solar light is used for photoactivation of oxides.

We used simulated Solar light in order to mimic conditions in natural waters. Here, the major role of ZrO_2 was to improve the adsorption characteristics of TiO_2 i.e. to increase the number of available active sites on binary oxide surface, compared to pure oxides, for the adsorption of pollutant molecules.

Phenol and its derivatives are common environmental pollutants,[28] so they were selected for study of the photocatalytic efficiencies of the synthesized samples. Kinetic curves of photocatalytic degradation of phenol are presented in Figure 6.

Figure 6. Kinetic curves of photocatalytic degradation of phenol on synthesized oxides

As can be seen in Figure 6, phenol was completely degraded after the first 180 min of illumination using TiO_2 as photocatalyst. Photocatalytic efficiency of TZ25 was lower compared to TiO_2; illumination induced desorption of phenol molecules from ZrO_2 surface.

Kinetic curves of photocatalytic degradation of 4-CP and TCP are presented in Figures 7a and 7b, respectively. In the first 120 min ZrO_2 and TZ25 have shown slightly better photocatalytic efficiency than pure TiO_2, Figure 7a. However, after this period, sharp increase of 4-CP concentration occurred in both zirconia containing samples, probably due to partial desorption of 4-CP from catalyst surface. Finally, all three samples exhibited similar photocatalytic activity after 240 min of illumination.

Fig. 7. Kinetic curves of photocatalytic degradation of a) 4-CP and b) TCP on synthesized oxides

Kinetic curves of photocatalytic degradation of TCP under simulated solar light are presented in Figure 7b. In the first 90 min of irradiation pure zirconia showed the best result for TCP removal, which was quite unexpected bearing in mind its wide band-gap. Additionally, photocatalytic activities of all coupled oxides were higher than that of pure TiO_2, and were as follows: ZrO_2 > TZ25>TZ50>TZ75>TiO_2.

After this initial 90 min, 40% of TCP was degraded by pure zirconia, while for all other samples this percent was less than 30. In the next 30 minutes, pure zirconia and all coupled oxides entered a kind of saturation, which can probably be explained with possible "contamination" of photocatalyst's surface by products of photodegradation of TCP. After this saturation period, reaction of photodegradation continued in the presence of pure zirconia and binary oxides. After 210 min of irradiation ZrO_2 and TZ25 degraded 70% of TCP, while in the cases of TZ50 and TZ75 it was about 62 and 52% of initial concentration, respectively. Concerning TiO_2, initial photodegradation was a bit sluggish, as if the catalyst needed more time to achieve adsorption/desorption equilibrium under applied irradiation. After 60 min, photocatalytic activity of TiO_2 steeply rose until 150 min, and then entered saturation.

Obviously, the high specific surface area (S_{BET}) cannot guarantee high photocatalytic activity; our results with TCP showed the opposite trend even as no clear correlation exists. We should bear in mind that our samples had small and comparable S_{BET} values (212-121 m^2 g^{-1}). Also, photocatalytic activity depends on the balance between the specific surface and the number of defects/active sites where reactions can take place as claimed in literature.[33,50]

Photocatalytic degradation certainly goes through oxidation of pollutant molecules by OH radicals, but route of OH radical's formation strongly depends on incident light energy and type of interaction between pollutant molecules and semiconductor surface. Adsorption of phenol and chlorophenols at the TiO_2/ZrO_2 surface is still subject of numerous studies. However, Agrios et al.[51] and Kim et al.[52] have studied photocatalytic degradation of phenol and phenolic compounds using TiO_2 under visible light illumination. They concluded that phenol and chlorophenols can be adsorbed on semiconductor surface through formation of charge-transfer (CT) complexes with phenolat linkage.[52] The type of electron coupling (weak/strong) between adsorbed molecule and semiconductor surface will determine process that will proceed after illumination. For strong electron coupling, direct transfer of the electron from the ligand molecule to the CB of the semiconductor is characteristic. This type of coupling is possible for ligands that contain two adjacent OH groups (or two donor groups)[9] that are then attached to neighbouring active sites, forming stable CT complexes.[7,8] In the case of weak electron coupling, the weakly chemisorbed molecule at the semiconductor surface is firstly excited, and then the electron gets transferred to the semiconductor.[9] Weak coupling has lower rates of back electron transfer.[9] For molecules like phenol and aliphatic alcohols, this type of monodentante coupling is the most probable, forming unstable complexes that can be photocatalyticaly degraded.

We believe that one of the reasons for differences in photocatalytic behaviour between TiO_2 and ZrO_2 in photocatalytic degradation of phenol and its derivatives can be ascribed to different coordination of surface metallic centres (explained earlier in text, subsection 3.1.) and consequently different stability of formed CT complexes.

Presence of chlorine in 4-CP and TCP drastically influenced formation of CT at the surface of ZrO_2 and TZ samples. As can be seen from kinetic curves (Figures 7a and b), ZrO_2 and TZ samples have shown better initial photocatalytic activity than pure TiO_2. Differences in efficiencies in the case of photocatalytic degradation of TCP are even more pronounced as it seems that the increased number of chlorine ions eases formation of CT complexes with ZrO_2 (Figure S3). According to Agrios et al.[51], increasing of the number of chlorines also leads to a shift of absorption edge of formed CT complexes towards longer wavelengths (lower energies), which can also be an additional explanation for better photocatalytic performance of ZrO_2 and TZ25 samples in the case of TCP, compared to 4-CP.

Conclusion

Pure ZrO_2 and TiO_2, as well as their mixed binary oxides with different ratios of ZrO_2 and TiO_2 were synthesized by solvothermal method. Pure ZrO_2 crystalizes predominantly in the metastable tetragonal crystal phase, with small additional content of the monoclinic crystal phase. TEM images revealed wide particle size distribution of irregularly shaped particles within this sample ranging from 2 to almost 30 nm. Pure TiO_2 predominantly crystalize in the anatase phase, with small additional content of brookite phase. Particle size distribution is very narrow, with the average particle size of about 7 nm. Upon influence of mixed water-isopropanol synthesis environment, TiO_2 crystallites have mixed spherical/cubic morphology. Upon mixing, both oxides kept the original crystalline and morphological characteristics. BET measurements revealed that the specific surface area rises from pure ZrO_2 to pure TiO_2, with the exception of TZ50 which had lower S_{BET} than pure ZrO_2. XPS measurements revealed that TZ25 has a surface with many defects which can be considered beneficial, as these defects induced energy levels placed within the band-gap of mixed oxide. UCPL spectra of all synthesized samples provided information about positions of these additional energy states, placing them at 3.08, 2.94, 2.77 and 2.56 eV. Additionally, XPS spectra of TZ75 and TZ25 gave evidence for ZrO_2- TiO_2 mixing. Band gap energies of all synthesized samples were estimated from Tauc plots; it was shown that both pure ZrO_2 and

TiO_2 have narrower band-gaps than reported bulk values: 4.1 and 3.0 eV respectively, and are shifted towards the visible part of spectra. All mixed oxides are characterized with a band-gap of about 3.1 eV. Photocatalytic activities under simulated solar light illumination of all samples were tested on phenol, 4-chlorophenol (4-CP) and 2,4,6-trichlorophenol (TCP). TiO_2 showed the highest photocatalytic activity in degradation of phenol; total degradation was obtained within 180 min. Pure ZrO_2 has shown no photocatalytic activity in degradation of phenol, moreover under simulated Solar light phenol starts to desorb from its surface. In the case of TCP, pure ZrO_2 and TZ25 degraded about 70% of the initial TCP concentration within 210 min, showing higher photocatalytic efficiency than TiO_2. Photoactivity of studied oxides under simulated Solar light illumination in photodegradation of phenol and its derivatives is discussed through formation of unstable CT complexes between pollutant molecules and oxides surface. Finally, we can conclude that oxides mixing can be beneficial for their photocatalytic activities, but their ratio must be adjusted according to type of pollutant that need to be degraded

Acknowledgements

The authors are grateful to Dr Miodrag Mitrić, Vinča Institute of Nuclear Sciences, Belgrade, Serbia, for XRD measurements; Prof. Vladimir B. Pavlović, Institute of Technical Sciences of SASA, Belgrade, Serbia, for TEM measurements; and Dr Janez Kovač, Jozef Stefan Institute, Ljubljana Slovenia, for XPS measurements. Financial support for this study was granted by the Ministry of Education, Science and Technological Development of the Republic of Serbia (Project OI172056).

Reference:

1. Hinojosa-Reyes L, Guzmán-Mar JL, Villanueva-Rodríguez M. Semiconductor materials for photocatalytic oxidation of organic pollutants in wastewater in: A. Hernández-Ramírez, I. Medina-Ramírez (Eds.), Photocatalytic semiconductors, Springer International Publishing Switzerland, 2015: 187-229.
2. Schneider J, Matsuoka M, Takeuchi M, et al. Understanding TiO_2 photocatalysis: mechanisms and materials. *Chem Rev.* 2014; 114: 9919–9986.
3. Xu H, Ouyang S, Liu L, et al. Recent advances in TiO_2-based photocatalysis. *J Mater Chem A.* 2014; 2:12642–12661.
4. Choi J, Perk H, Hoffmann MR. Effects of single metal-ion doping on the visible-light photoreactivity of TiO_2. *J Phys Chem C.* 2010; 114: 783–792.
5. Abazović ND, Čomor MI, Zec S, et al. Structural and optical characterization of flower-like rutile nanostructures doped with Fe^{3+}. *J Am Ceram Soc*. 2009; 92(4): 894–896.
6. Manu S, Abdul Khadar M. Non-uniform distribution of dopant iron ions in TiO_2 nanocrystals probed by X-ray diffraction, Raman scattering, photoluminescence and photocatalysis. *J Mater Chem C.* 2015; 3:1846–1853.
7. Rajh T, Chen LX, Lukas K, et al. Surface restructuring of nanoparticles: An efficient route for ligand−metal oxide crosstalk. *J Phys Chem B.* 2002; 106: 10543-10552.
8. Radoičić MB, Janković IA, Despotović VN, et al. The role of surface defect sites of titania nanoparticles in the photocatalysis: Aging and modification. *App Catal B – Environ.* 2013; 138–139:122–127.
9. Macyk W, Szaciłowski K, Stochel G, et al. Titanium (IV) complexes as direct TiO_2 photosensitizers. *Coordin Chem Rev*. 2010; 254: 2687–2701.

10. Aman N, Das NN, Mishra T. Effect of N-doping on visible light activity of TiO_2–SiO_2 mixed oxide photocatalysts. *J Environ Chem Eng*. 2016; 4:191–196.
11. Rasalingam S, Peng R, Koodali RT. Removal of hazardous pollutants from wastewaters: Applications of TiO_2-SiO_2 mixed oxide materials. *J Nanomater*. 2014: 617405.
12. Polat M, Soylu AM, Erdogan DA, et al. Influence of the sol–gel preparation method on the photocatalytic NO oxidation performance of TiO_2/Al_2O_3 binary oxides. *Catal Today*. 2015; 241: 25–32.
13. Soylu AM, Polat M, Erdogan DA, et al. TiO_2–Al_2O_3 binary mixed oxide surfaces for photocatalytic NO_x abatement. *App Surf Sci*. 2014; 318:142–149.
14. Pozan GS, Kambur A, Significant enhancement of photocatalytic activity over bifunctional ZnO–TiO_2 catalysts for 4-chlorophenol degradation. *Chemosphere*. 2014; 105:152–159.
15. Lv P, Zheng M, Wang X, Huang F. Subsolidus phase relationships and photocatalytic properties in the ternary system TiO_2–Bi_2O_3–V_2O_5. *J Alloy Compd*. 2014; 583: 285–290.
16. Pirzada BM, Mir NA, Qutub N, et al. Synthesis, characterization and optimization of photocatalytic activity of TiO_2/ZrO_2 nanocomposite heterostructures. *Mat Sci Eng B*. 2015; 193:137-145.
17. Khan S, Kim J, Sotto A, Van der Bruggen B. Humic acid fouling in a submerged photocatalytic membrane reactor with binary TiO_2–ZrO_2 particles. *J Ind Eng Chem*. 2015; 2:779-785.
18. Lukáč J, Klementová M, Bezdička P, et al. Influence of Zr as TiO_2 doping ion on photocatalytic degradation of 4-chlorophenol. *App Catal B- Environ*. 2007; 74: 83–91.

19. Liu H, Su Y, Hu H, et al. An ionic liquid route to prepare mesoporous ZrO_2–TiO_2 nanocomposites and study on their photocatalytic activities. *Adv Powder Technol.* 2013; 24: 683-688.
20. Mazurkevich YS, Kobasa IM. ZrO_2–TiO_2 Materials. *Inorg Mater*. 2001; 37:1285-1288.
21. Zou H, Lin YS. Structural and surface chemical properties of sol–gel derived TiO_2–ZrO_2 oxides. *App Catal A- Gen*. 2004; 265: 35-42.
22. Kambur A, Pozan GS, Boz I. Preparation, characterization and photocatalytic activity of TiO_2–ZrO_2 binary oxide nanoparticles. *App Catal B – Environ*. 2012; 115-116: 149-158.
23. Onsuratoom S, Chavadej S, Sreethawong T. Hydrogen production from water splitting under UV light irradiation over Ag-loaded mesoporous-assembled TiO_2-ZrO_2 mixed oxide nanocrystal photocatalysts. *Int J Hydogen Energ*. 2011; 36: 5246-5261.
24. Gionco C, Battiato A, Vittone E, et al. Structural and spectroscopic properties of high temperature prepared ZrO_2–TiO_2 mixed oxides. *J Solid State Chem*. 2013; 201:222-228.
25. Pérez-Hernández R, Mendoza-Anaya D, Fernández ME, et al. Synthesis of mixed ZrO_2–TiO_2 oxides by sol–gel: Microstructural characterization and infrared spectroscopy studies of NO_x. *J Mol Catal A- Chem*. 2008; 281: 200-206.
26. Rtimi S, Pulgarin C, Sanjines R, Kiwi J. Accelerated self-cleaning by Cu promoted semiconductor binary-oxides under low intensity sunlight irradiation. *App Catal B – Environ.* 2016; 180: 648-655.
27. Rtimi S, Pulgarin C, Sanjines R, et al. Preparation and mechanism of Cu-decorated TiO_2–ZrO_2 films showing accelerated bacterial inactivation. *ACS Appl Mater Interfaces*. 2015; 7:12832–12839.

28. Dionysiou DD, Khodadoust AP, Kern AM, et al. Continuous-mode photocatalytic degradation of chlorinated phenols and pesticides in water using a bench-scale TiO_2 rotating disk reactor. *App Catal B – Environ.* 2000; 24: 139–155.
29. Rouquerol F, Rouquerol J, Sing KSW, et al. Adsorption by powders and porous solids, principles, methodology and applications, Academic Press, New York, 2012.
30. Lippens BC, Linsen BG and de Boer JH. Studies on pore systems in catalysis I. The adsorption of nitrogen; apparatus and calculation. *J Catal.* 1964; 3: 32.
31. Sing K, Everet D, Haul R et al. Reporting physisorption datafor gas/solid systems. *Pure Appl Chem.* 1985; 57: 603.
32. Radoičić M, Šaponjić Z, Janković IA, et al. Improvements to the photocatalytic efficiency of polyaniline modified TiO_2 nanoparticles. *Appl Cat B- Environ.* 2013; 136-137: 133-139.
33. Carević MV, Abazović ND, Novaković TB, et al. Zirconium dioxide nanopowders with incorporated Si^{4+} ions as efficient photocatalyst for degradation of trichlorophenol using simulated solar light. *Appl Cat B- Environ.* 2016; 195: 112–120.
34. Di Paola A, Bellardita M, Palmisano L. Brookite, the least known TiO_2 photocatalyst. *Catalysts*. 2013; 3: 36-73.
35. Hanaoar DA, Sorrell CC. Review of the anatase to rutile phase transformation. *J Mater Sci*. 2011; 46: 855-874.
36. Hurum DC, Agrios AG, Gray KA et al. Explaining the enhanced photocatalytic activity of Degussa P25 mixed-phase TiO_2 Using EPR. *J Phys Chem B*. 2003; 107: 4545-4549.
37. Yamaguchi T. Application of ZrO_2 as a catalyst and a catalyst support. *Catal. Today*. 1994; 20: 199-218.

38. Chang S, Doong R. Chemical-composition-dependent metastability of tetragonal ZrO_2 in sol-gel-derived films under different calcination conditions. *Chem Mater*. 2005; 17: 4837-4844.

39. Monte F, Larsen W, Mackenzie JD. Stabilization of tetragonal ZrO_2 in ZrO_2–SiO_2 binary oxides. *J Am Ceram Soc*. 2000; 83: 628–634

40. Shuang Y, Hou Y, Zhang B, Yang HG. Impurity-free synthesis of cube-like single-crystal anatase TiO_2 for high performance dye-sensitized solar cell. *Ind Eng Chem Res.* 2013; 52: 4098−4102.

41. Xu Q, Yu J, Zhang J, et al. Cubic anatase TiO_2 nanocrystals with enhanced photocatalytic CO_2 reduction activity. *Chem Commun.* 2015; 51: 7950-7953.

42. Rignanese G-M. Dielectric properties of crystalline and amorphous transition metal oxides and silicates as potential high-κ candidates: the contribution of density-functional theory. *J Phys: Condens Matter.* 2005;17: R357–R379.

43. NIST X-ray photoelectron spectroscopy database, NIST Standard Reference Database 20, Version 4.1, http://srdata.nist.gov/xps/Default.aspx

44. Wang QM, Gong J, Sun C, et al. ZrO_2 and Y_2O_3-stablized ZrO_2 coatings deposited using an arc ion plating technique. *J Ceram Process Res*. 2011; 12: 259 – 264.

45. Abazović ND, Čomor MI, Dramićanin MD, et al. Photoluminescence of anatase and rutile TiO_2 particles. *J Phys Chem B.* 2006; 110: 25366-25370.

46. Wang Z, Yang B, Fu Z, et al. UV–blue photoluminescence from ZrO_2 nanopowders prepared via glycine nitrate process. *Appl Phys A.* 2005; 81: 691–694.

47. Liang J, Deng Z, Jiang X, Li F, et al. Photoluminescence of tetragonal ZrO_2 nanoparticles synthesized by microwave irradiation. *Inorg Chem.* 2002; 41: 3602−3604.

48. Xu X. and Wang X. Fine tuning of the sizes and phases of ZrO_2 nanocrystals. *Nano Res*. 2009; 2: 891-902.
49. Carvalho JM, Rodrigues LCV, M. C. F. C. Felinto MCFC, et al. Structure–property relationship of luminescent zirconia nanomaterials obtained by sol–gel method. *J Mater Sci*. 2015; 50: 873–881.
50. Carević MV, Abazović ND, Savić TD, et al. Structural, optical and photodegradation properties of pure and Fe-doped titania nanoparticles probed using simulated Solar light, *Ceram Int.* 2016; 42: 1521–1529.
51. Agrios AG, Gray KA, Weitz E. Narrow-band irradiation of a homologous series of chlorophenols on TiO_2: charge-transfer complex formation and reactivity. *Langmuir*. 2004; 20: 5911-5917.
52. Kim S, Choi W. Visible-light-induced photocatalytic degradation of 4-chlorophenol and phenolic compounds in aqueous suspension of pure titania: demonstrating the existence of a surface-complex-mediated path *J Phys Chem B.* 2005; 109: 5143-5149.

Figure Captions

Figure 1. XRD patterns of pure and binary oxides

Figure 2. TEM images of synthesized oxides: a) TiO_2, b) ZrO_2, c) TZ25, d) TZ50 and e) TZ75

Figure 3. a) N_2 adsorption/desorption isotherms and (b) pore size distributions patterns of synthesized oxides.

Figure 4. XPS spectra and their deconvolutions of the characteristic energy ranges: Ti 2p binding energies for TZ25 (a) and TZ75 (b), Zr 3d energy ranges for TZ25 (c) and TZ75 (d) and O 1s binding energy ranges for TZ25 (e) and TZ75 (f).

Figure 5. a) DRS spectra (inset: Tauc plots); b) PL spectra and c) UCPL spectra of synthesized oxides.

Figure 6. Kinetic curves of photocatalytic degradation of phenol on synthesized oxides.

Figure 7. Kinetic curves of photocatalytic degradation of a) 4-CP and b) TCP on synthesized oxides.

Table 1. Amounts of TTIP and ZIP used for oxides synthesis

Sample	TTIP (ml)	ZIP (ml)
TiO_2	4	-
TZ25	3	1.43
TZ50	2	2.85
TZ75	1	4.29
ZrO_2	-	5.7

Table 2. Textural properties of synthesized oxides

Sample	S_{BET} (m^2g^{-1})	$V_{p\ 0.98}$ (cm^3g^{-1})	Pore size (nm)
TiO_2	212	0.296	5.5
TZ25	204	0.287	5.4
TZ50	121	0.174	5.2
TZ75	144	0.222	4.8
ZrO_2	123	0.144	4.5

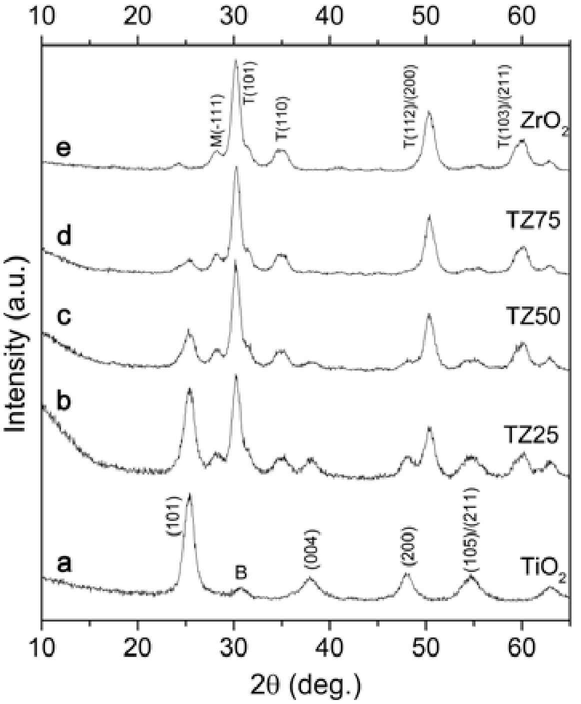
10
20
30
40
50
60
e
M(-111)
T(101)
T(110)
T(112)/(200)
T(103)/(211)
ZrO_2
d
TZ75
c
TZ50
b
TZ25
a
(101)
B
(004)
(200)
(105)/(211)
TiO_2
Intensity (a.u.)
2θ (deg.)

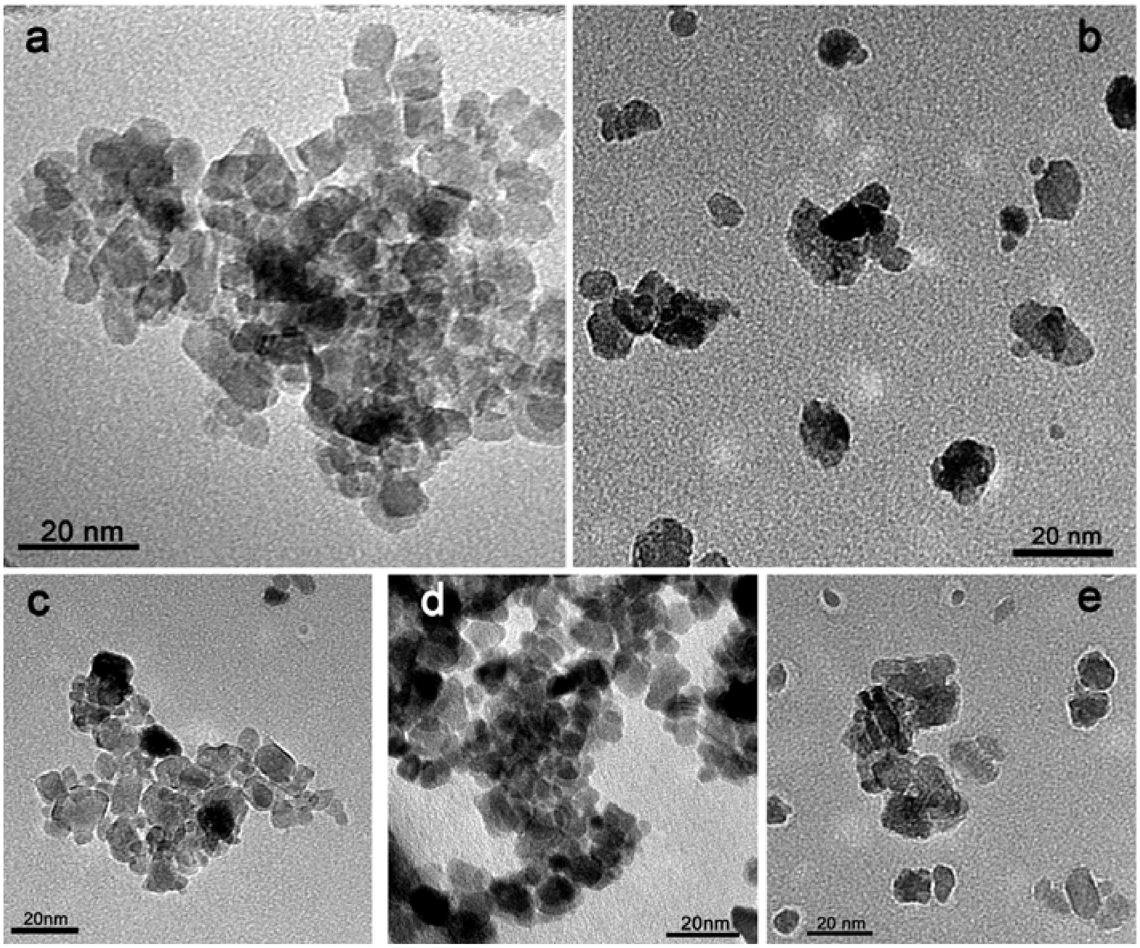
a
20 nm
b
20 nm
c
20nm
d
20nm
e
20 nm

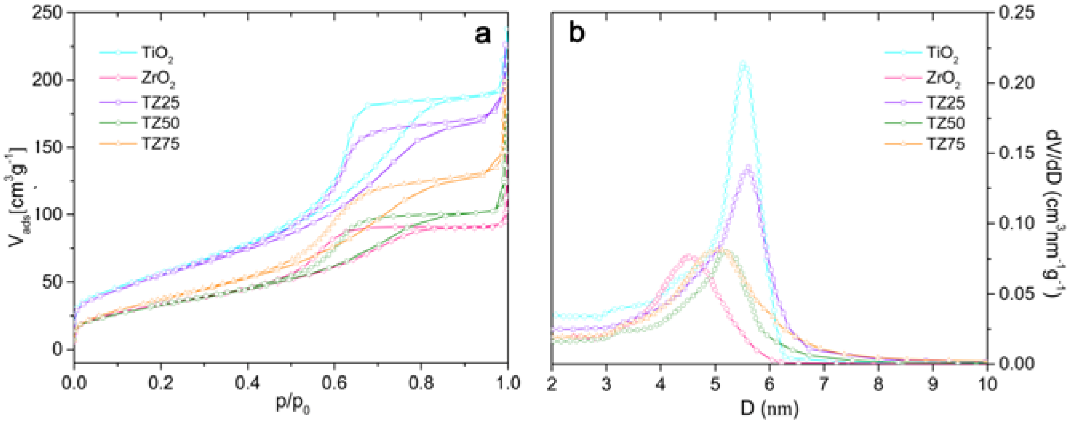
a
V_{ads} [cm^{3}g^{-1}]
p/p$_0$
0
50
100
150
200
250
0.0
0.2
0.4
0.6
0.8
1.0
TiO$_2$
ZrO$_2$
TZ25
TZ50
TZ75
b
dV/dD (cm^{3}nm^{-1}g^{-1})
D (nm)
0.00
0.05
0.10
0.15
0.20
0.25
2
3
4
5
6
7
8
9
10
TiO$_2$
ZrO$_2$
TZ25
TZ50
TZ75

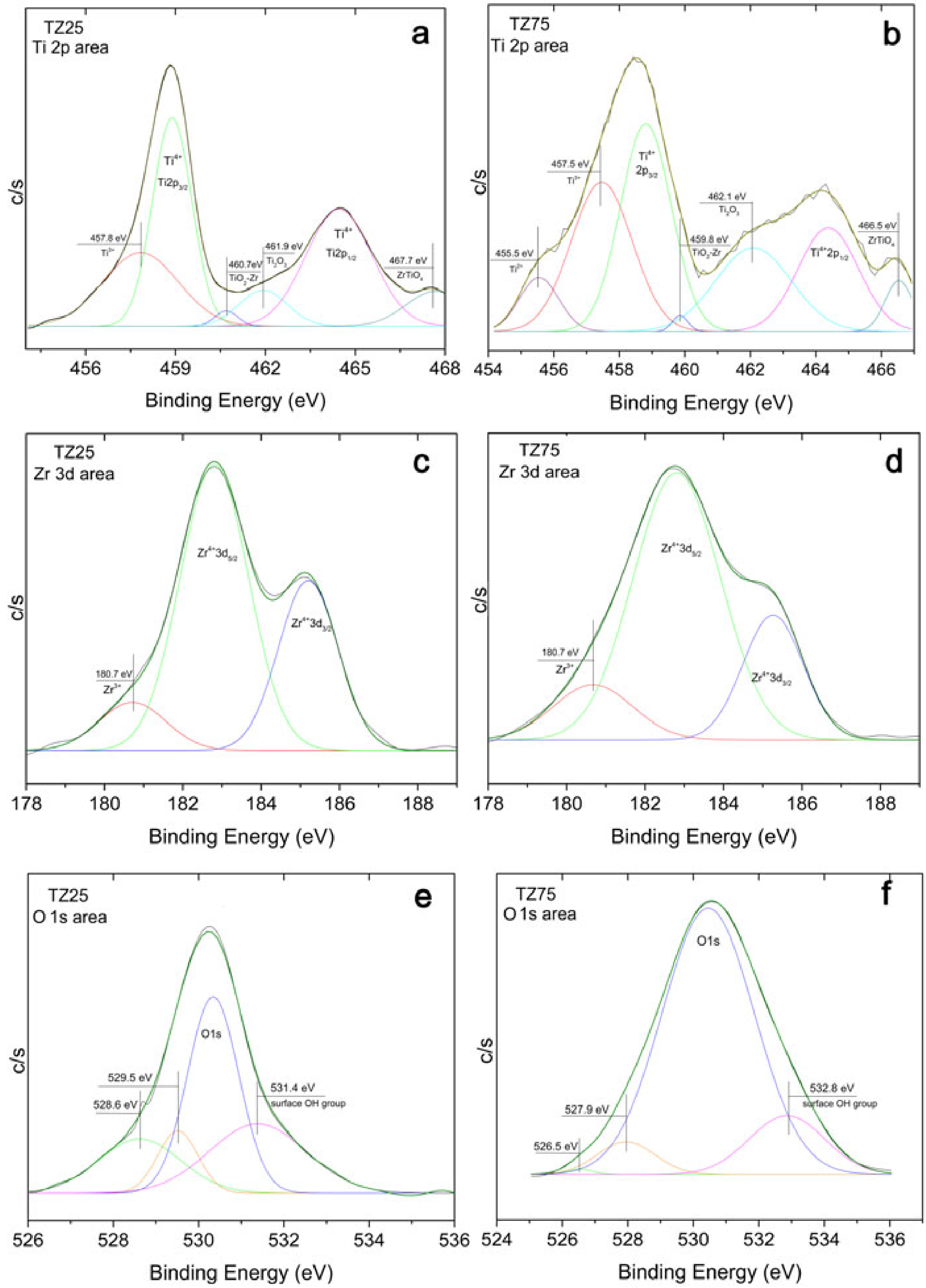
TZ25
Ti 2p area
a
c/s
457.8 eV
Ti^{3+}
Ti^{4+}
$Ti2p_{3/2}$
460.7eV
TiO_2-Zr
461.9 eV
Ti_2O_3
Ti^{4+}
$Ti2p_{1/2}$
467.7 eV
$ZrTiO_4$
456
459
462
465
468
Binding Energy (eV)
TZ75
Ti 2p area
b
c/s
455.5 eV
Ti^{2+}
457.5 eV
Ti^{3+}
Ti^{4+}
$2p_{3/2}$
459.8 eV
TiO_2-Zr
462.1 eV
Ti_2O_3
$Ti^{4+}2p_{1/2}$
466.5 eV
$ZrTiO_4$
454
456
458
460
462
464
466
Binding Energy (eV)
TZ25
Zr 3d area
c
c/s
180.7 eV
Zr^{3+}
$Zr^{4+}3d_{5/2}$
$Zr^{4+}3d_{3/2}$
178
180
182
184
186
188
Binding Energy (eV)
TZ75
Zr 3d area
d
c/s
180.7 eV
Zr^{3+}
$Zr^{4+}3d_{5/2}$
$Zr^{4+}3d_{3/2}$
178
180
182
184
186
188
Binding Energy (eV)
TZ25
O 1s area
e
c/s
529.5 eV
528.6 eV
O1s
531.4 eV
surface OH group
526
528
530
532
534
536
Binding Energy (eV)
TZ75
O 1s area
f
c/s
O1s
527.9 eV
526.5 eV
532.8 eV
surface OH group
524
526
528
530
532
534
536
Binding Energy (eV)

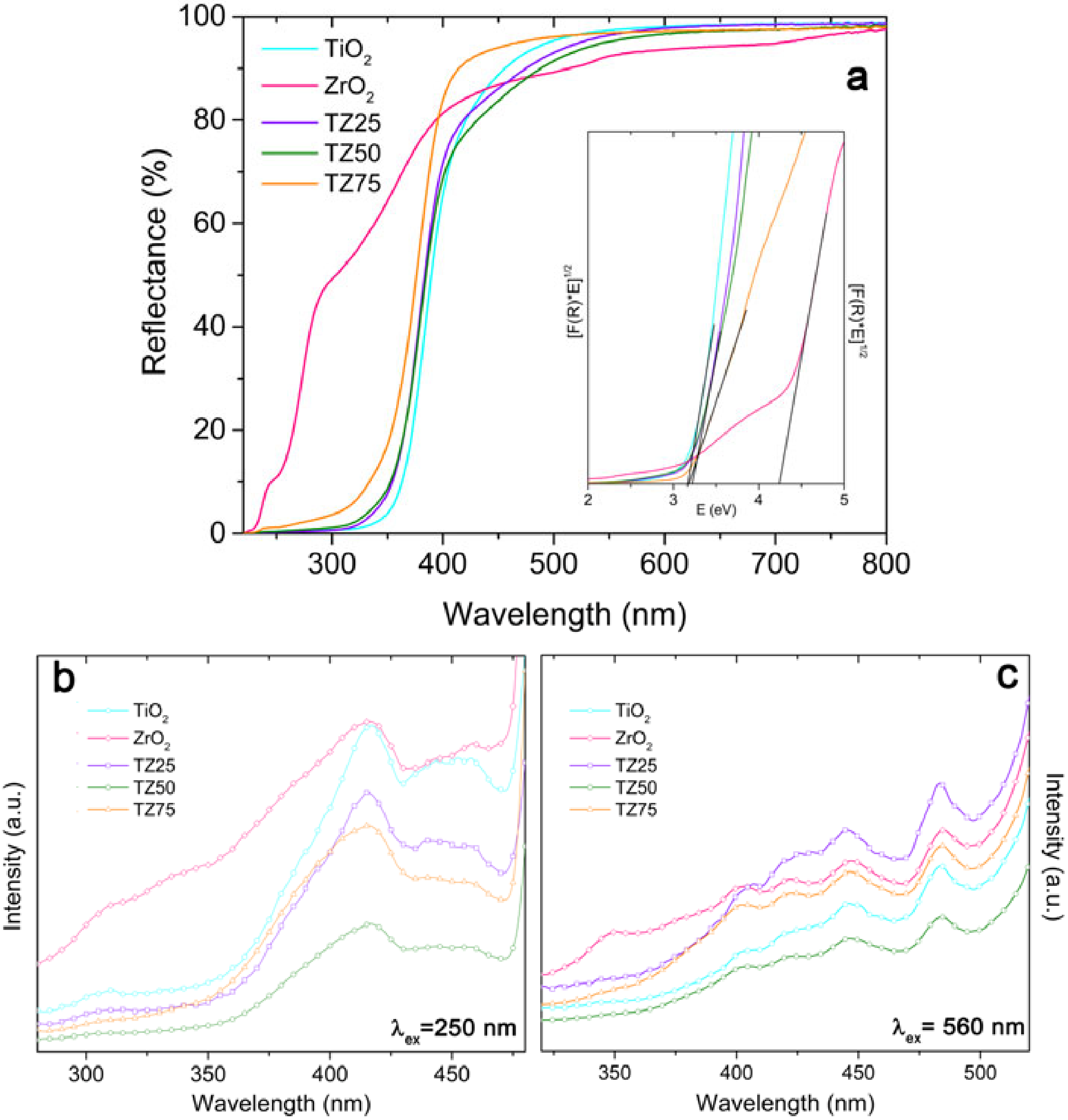
a
Reflectance (%)
0
20
40
60
80
100
300
400
500
600
700
800
Wavelength (nm)
TiO2
ZrO2
TZ25
TZ50
TZ75
[F(R)*E]1/2
[F(R)*E]1/2
E (eV)
2
3
4
5
b
Intensity (a.u.)
TiO2
ZrO2
TZ25
TZ50
TZ75
λex=250 nm
300
350
400
450
Wavelength (nm)
c
Intensity (a.u.)
TiO2
ZrO2
TZ25
TZ50
TZ75
λex= 560 nm
350
400
450
500
Wavelength (nm)

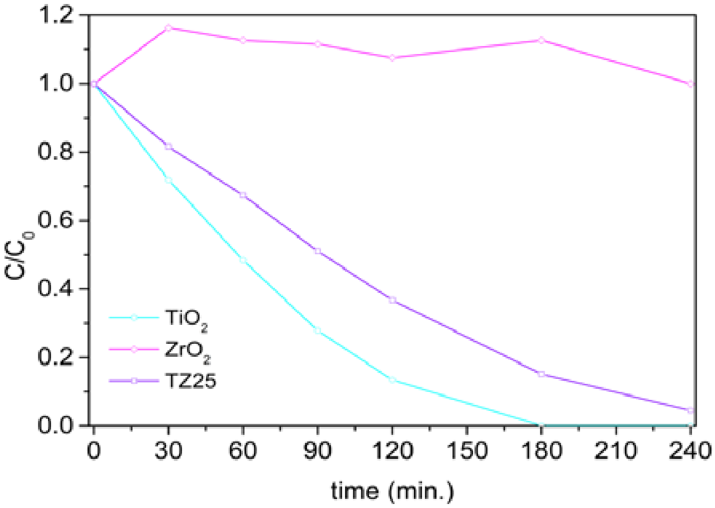
1.2
1.0
0.8
0.6
0.4
0.2
0.0
C/C0
0
30
60
90
120
150
180
210
240
time (min.)
TiO2
ZrO2
TZ25

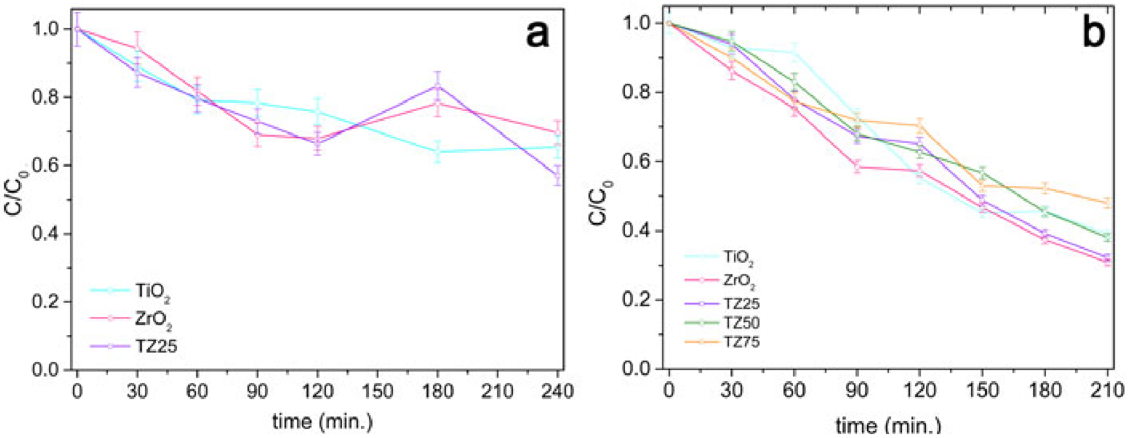
a
1.0
0.8
0.6
0.4
0.2
0.0
C/C0
0
30
60
90
120
150
180
210
240
time (min.)
TiO2
ZrO2
TZ25
b
1.0
0.8
0.6
0.4
0.2
0.0
C/C0
0
30
60
90
120
150
180
210
time (min.)
TiO2
ZrO2
TZ25
TZ50
TZ75